Coupled Confined Phase Behavior and Transport of

Methane in Slit Nanopores

Yuhang Wang^a, Saman A. Aryana^{b,c,*}

^aDepartment of Petroleum Engineering, University of Wyoming, Laramie, WY 82071, USA

^bDepartment of Chemical Engineering, University of Wyoming, Laramie, WY 82071, USA

^cDepartment of Mathematics and Statistics, University of Wyoming, Laramie, WY 82071, USA

https://doi.org/10.1016/j.cej.2020.126502

Abstract

The proximity of the order of magnitude molecular mean free path and pore sizes

in nanopores leads to remarkable interactions between molecules and walls. In

such systems, the thermodynamic property and the transport behavior of fluids

deviate from those at bulk conditions. Molecular dynamics (MD) simulation

may be used to investigate the effects of confinement on fluid physics in nano-

size pores. However, translating these subscale observations into a larger scale

of interest remains a challenging task. In this work, we propose a modified

extension of Peng-Robinson equation of state (PR-EOS) motivated and guided

by MD simulation results. The shift of critical properties, i.e., pressure and

temperature, are evaluated independently. A temperature dependent parameter

is introduced to account for the existence of capillary pressure in the two-phase

region. This formulation is capable of capturing the shift in critical properties

as well as density phase diagrams under various confinement scenarios. We

incorporate the proposed EOS in the lattice Boltzmann method (LBM) to study

*Corresponding author

 $Email\ address:\ {\tt saryana@uwyo.edu}\ ({\tt Saman\ A.\ Aryana}\)$

coupled confined phase behavior and transport of methane in nano-size slit pores. Adsorptive strength is determined such that the resulting density ratio matches that from MD simulation. Results indicate that the use of the proposed EOS leads to smaller fluid velocities compared to PR-EOS. This effect is due to stronger interactions between fluid particles under confinement. Also, results show that transport characteristics are impacted by the pressure of the system: in systems with a relatively low pressure, transport seems to be dominated by Knudsen diffusion; however, at a higher pressure, the contribution from viscous flow increases as the pore widens while the influence of Knudsen and surface diffusion diminishes.

Keywords: Confined phase behavior, Equation of state, Rarefied gas flow,

Lattice Boltzmann method

1. Introduction

Shale gas, which is composed of methane primarily, is an unconventional resource that has become a significant source of natural gas due to the advancements in stimulation techniques. The transport process of methane is in general a multi-scale process: methane flows through the organic nanopores, followed by the fracture network, and eventually into the wellbore. Despite great advances in discretization schemes for simulating flow in fractured reservoirs [1, 2, 3, 4, 5, 6], and predictions of pore pressure and stress field via coupling of flow and geomechanics using the model proposed by Biot [7, 8, 9, 10], the transport mechanism of shale gas in the matrix, where a majority of pores are nano-size [11, 12, 13, 14], may not be fully understood. Under such confined

conditions, measuring fluid properties or visualizing fluid flow via experimental techniques is a challenging task. On the other hand, numerical simulation becomes an efficient alternative. This work focuses on developing a physics-based description for confined phase behavior of methane, and on coupling the developed formulation with a transport model to investigate pore-scale transport characteristics under confinement.

Selecting an appropriate simulation approach that fits the underlying flow regimes is of great significance for accuracy and efficiency. As classified by Knudsen number, defined as the ratio of molecular mean free path to the characteristic length of flow field, methane flow in those nanopores are often considered to be in either slip flow or transitional flow regime, in which the continuum-based approach may not be valid. As a result, a particle-based approach may be more appropriate for such systems. Molecular dynamics (MD) simulation is able to capture the dynamics at molecular level accurately, because it focuses on exact interactions between molecules. This technique has been applied to investigate the transport of hydrocarbon in microscopic systems. Falk et al. [15] simulated mass transport of condensed hydrocarbons in a nanoporous carbon matrix using grand canonical Monte Carlo (GCMC) MD simulation. Results indicate that Darcy's law fails to predict the transport of hydrocarbons in nanoporous matrix. Riewchotisakul and Akkutlu [16] presented the results of methane flow in nanotubes using the nonequilibrium MD simulation. They identified that the adsorbed phase is mobile, which contributes to the overall transport significantly. Yu et al. [17] investigated pressure dependent transport characteristics of methane in slit nanopores using MD simulation, and proposed an analytical formulation used to predict the apparent permeability.

With the help of MD simulation, the physics that governs flow and transport at microscale are revealed. Nonetheless, an increase in the fluid complexity or system size poses a serious challenge for MD simulation due to the required computational power and complexity of the force field. One possible remedy would be to leverage findings from MD simulation and develop a mesoscopic computational model [18]. Such a method must capture small scale physics satisfactorily and enable translation of scales from a microscopic level to macroscale. To that end, this work uses the lattice Boltzmann method (LBM). The governing equation of LBM is the discrete form of Boltzmann equation, which assimilates the essential physics and neglects molecular level interactions [19, 20]. Interplay between fluid molecules, and between fluid molecules and walls, is incorporated in the form of external forces that act on the particles represented by the density distribution function. Shan and Chen [21] introduced a long-range interaction force between particles which is dependent on the pseudopotential function of fluid particles. Sukop and Or [22] proposed an interaction force between particles and walls to study interface configurations in partially saturated porous media. Fathi and Akkutlu [23] and Ning et al. [24] applied this force term to capture the adsorbed gas in kerogen nanotubes, where the adsorptive forces are also expressed as a function of pseudopotential.

Determination of the pseudopotential function requires a suitable equation of state (EOS) [25], which describes the relation of pressure, temperature, and

density for a given substance. Previous studies have incorporated different forms of EOS into the LBM. Examples include the van der Waals (vdW)-EOS [24, 26], and the Peng-Robinson (PR)-EOS [27, 28, 29], which is one of the prominent EOS for natural gas systems. These two non-ideal EOS, wihch account for interactions of fluid molecules at bulk condition, may not be valid in confined space. As summarized by Liu and Zhang [30], two distinct phenomena are observed in fluids under confinement: a) appearance of capillary pressure between vapor and liquid phases, and b) shift of the critical point. Since PR-EOS is used to describe phase behavior of bulk fluids, a popular correction, when applying PR-EOS to confined fluids, is to include capillary pressure in flash calculations for multicomponent systems [31, 32]. This correction in general leads to a suppressed bubble point pressure. Nonetheless, inclusion of capillary pressure does not capture the shift of critical point because capillary pressure vanishes at the critical point. To remedy the inconsistency, this correction is often combined with a shift of critical point in flash calculation [33, 34, 35]. The shift of critical properties, e.g., pressure and temperature, are obtained either from analytical derivations [36], or MD simulation [37, 38, 39, 40, 41]. The GCMC, or modified gauge-GCMC MD simulation has been used to study the thermodynamics of confined fluids [39, 40]. Sobecki et al. [41] pointed out that determination of chemical potential with respect to condensation using GCMC remains a challenging task. This issue is, however, resolved in the Gibbs ensemble Monte Carlo (GEMC) method [42, 43].

This work seeks an explicit formulation for EOS that captures confined phase

behavior for pure fluids, namely, methane. Derouane [44] proposed a modified vdW-EOS that incorporates fluid-wall interactions by reducing the correction term regarding internal pressure. This model gives a reduced critical temperature and an increased critical pressure, which are inconsistent with observations obtained from MD simulation. Yang et al. [45] proposed an extension of PR-EOS, referred to as EPR-EOS, by introducing a new term in PR-EOS accounting for interactions between molecules and walls. The introduced parameter is determined based on data collected from experiment and MD simulation. This extension provides a simple and efficient formulation in dealing with the shift of critical properties. In this extension, the following two points may deserve further discussion. First, only the shift in the critical temperature is used for establishing the parameter. As a consequence, critical pressure is shifted at the same ratio as the critical temperature, which may not be necessarily true as observed from MD simulation results [41]. Second, the proposed EPR-EOS is applied to studying multicomponent systems directly whereas the validity of this model for a single component is not fully investigated. To gain more insight into the applicability of PR-EOS to confined phase behavior, these two points will be discussed and addressed in this work.

In the remainder of this paper, we first present different forms of EOS, including PR-EOS, EPR-EOS and the proposed mEPR-EOS. Analytical expressions for critical pressure and temperature obtained from different EOS are derived and compared. We then describe the governing equation for the multiple relaxatio time (MRT)-LBM. The combined half-way bounce-back and specular

reflection boundary treatment is utilized to capture the slip velocity. The pseudopotential function, which is incorporated into the interparticle and surface forces, are derived based on mEPR-EOS. Next, we present the motivation and formulation of the developed mEPR-EOS. A new parameter is proposed that accounts for the existence of capillary pressure in the two-phase region. We validate the model by comparing numerical solutions of mEPR-EOS with the reference data. We couple mEPR-EOS with MRT-LBM to investigate the effects of confined phase behavior on transport of methane in slit nanopores, and analyze the transport characteristics based on mass flux profiles. We close with a discussion of the results and conclusions.

2. Method

2.1. Equation of State

PR-EOS, which is the basis of this work, is expressed as [27]

$$P = \frac{RT}{v - b} - \frac{a}{v^2 + 2bv - b^2},\tag{2.1}$$

where

$$a = 0.45724 \frac{R^2 T_{cb}^2}{P_{cb}} \alpha, (2.2)$$

$$b = 0.0778 \frac{RT_{cb}}{P_{cb}},\tag{2.3}$$

and

$$\alpha = \left[1 + \left(0.37464 + 1.54226\omega - 0.26992\omega^2\right) \left(1 - \sqrt{T_r}\right)\right]^2. \tag{2.4}$$

In this system (Eqs. (2.1) to (2.4)), subscript 'cb' denotes critical property at bulk condition, P and T are pressure and temperature, respectively, v is molar

volume, R is the universal gas constant, a and b are parameters associated with attractive and repulsive forces, respectively, and α is a dimensionless parameter describing the dependence of attractive parameter, a, on temperature and shape of molecules through reduced temperature, T_r , and acentric factor, ω .

The critical isotherm of a pure substance has a point of inflection at the critical point. This condition indicates that the first and second derivatives of pressure with respect to molar volume at the critical point, i.e., $P = P_{cb}$, and $T = T_{cb}$, are equal to zero, which are expressed as

$$\left(\frac{\partial P}{\partial v}\right)_{P_{ch}, T_{ch}} = \left(\frac{\partial^2 P}{\partial v^2}\right)_{P_{ch}, T_{ch}} = 0.$$
(2.5)

 P_{cb} and T_{cb} are derived by imposing conditions of Eq. (2.5) on Eq. (2.1), which are given by

$$P_{cb} = 0.01324 \frac{a}{\alpha h^2},\tag{2.6}$$

and

$$T_{cb} = 0.17015 \frac{a}{\alpha b R}.$$
 (2.7)

Yang et al. [45] proposed the EPR-EOS by subtracting c from the attractive parameter:

$$P = \frac{RT}{v - b} - \frac{a - c}{v^2 + 2bv - b^2}. (2.8)$$

Based on Eq. (2.5), the critical pressure and temperature of EPR-EOS is given by

$$P_{ce} = 0.01324 \frac{a - c}{\alpha b^2},\tag{2.9}$$

and

$$T_{ce} = 0.17015 \frac{a - c}{\alpha bR},\tag{2.10}$$

where subscript 'ce' denote critical property obtained using EPR-EOS. Here the shift of property at critical point, defined as the ratio of critical property in confined space over that of the bulk condition, is used to quantify the evolution of critical properties with confinement. Combining Eqs. (2.6), (2.7), (2.9), and (2.10), the shift of critical properties using EPR-EOS are given by

$$\frac{P_{ce}}{P_{cb}} = \frac{T_{ce}}{T_{cb}} = \frac{a - c}{a}.$$
 (2.11)

Eq. (2.11) indicates that critical pressure and temperature are shifted at the same ratio, and the magnitude of shift is controlled by parameter c.

We propose a modified EPR-EOS, referred to as mEPR-EOS, in which shift of critical properties, i.e., pressure and temperature, are evaluated independently. A new parameter, β , which is used to describe the shift of critical pressure, is introduced. The resulting EOS is expressed as

$$P = \frac{RT}{v - b'} - \frac{a' - c'}{v^2 + 2bv - b^2},\tag{2.12}$$

where

$$a' = \frac{a}{\beta}$$
, $b' = \frac{b}{\beta}$, and $c' = \frac{c}{\beta}$. (2.13)

The critical pressure and temperature of mEPR-EOS is given by

$$P_{cm} = 0.01324 \frac{a' - c'}{\alpha b'^2},\tag{2.14}$$

and

$$T_{cm} = 0.17015 \frac{a' - c'}{\alpha b' R},\tag{2.15}$$

where subscript 'cm' denote critical property obtained using mEPR-EOS. Combining Eqs. (2.6), (2.7), (2.11), (2.14), and (2.15), we show that the shift critical

temperature using mEPR-EOS is the same as that of EPR-EOS:

$$\frac{T_{cm}}{T_{cb}} = \frac{T_{ce}}{T_{cb}} = \frac{a-c}{a},\tag{2.16}$$

meanwhile the shift of critical pressure is different:

$$\frac{P_{cm}}{P_{cb}} = \frac{a-c}{a}\beta. \tag{2.17}$$

Value of parameter c is determined based on the reference data, which may be obtained from experimental measurements or MD simulation results, as given by

$$c = (1 - T_{cr}) a, (2.18)$$

where subscript 'cr' denotes the reference value of the shift of critical property. Formulation of β will be discussed in detail in the following section.

2.2. Lattice Boltzmann method

2.2.1. Governing Equation

The lattice Boltzmann equation, derived from the continuous Boltzmann equation [46], is given by

$$f_i(\mathbf{x} + c\mathbf{e}_i\delta t, t + \delta t) - f_i(\mathbf{x}, t) = \Omega_i(f(\mathbf{x}, t)) + \delta t F_i(\mathbf{x}, t), \qquad (2.19)$$

where subscript i denotes the index of discrete velocities, $f_i(\boldsymbol{x},t)$ is the discrete distribution function along i-direction at time t and position \boldsymbol{x} . Eq. (2.19) indicates that fluid is simulated as particles represented by $f_i(\boldsymbol{x},t)$ which flows along a discrete lattice. Here we use two-dimensional, nine-velocity (D2Q9) lattice model, where the discrete velocities are given by $\boldsymbol{e}_0 = (0,0), \, \boldsymbol{e}_1 = -\boldsymbol{e}_3 = 0$

 $(1,0), e_2 = -e_4 = (0,1), e_5 = -e_7 = (1,1), \text{ and } e_6 = -e_8 = (-1,1). c \text{ is the lattice speed defined as the ratio of lattice spacing, } \delta x, \text{ over the time step, } \delta t,$ and it is set to 1. $\Omega_i(f(\boldsymbol{x},t))$ is the collision operator representing the rate of change of f_i resulting from collision, and $F_i(\boldsymbol{x},t)$ is the forcing term accounting for the body force G.

The MRT collision operator is implemented, in which $\Omega_i(f)$ is given by [47, 48]

$$\Omega_{i}(f) = -\sum_{j} \left(\mathbf{M}^{-1} \mathbf{S} \mathbf{M} \right)_{ij} \left(f_{j} - f_{j}^{\text{eq}} \right), \qquad (2.20)$$

where $f = f(\boldsymbol{x}, t)$. \boldsymbol{M} is a transformation matrix projecting the discrete distribution functions onto the moment space [47], i.e., $\boldsymbol{m} = \boldsymbol{M}\boldsymbol{f}$, where $\boldsymbol{f} = (f_0, f_1, ..., f_8)^T$. \boldsymbol{S} is a diagonal matrix given by

$$\mathbf{S} = \operatorname{diag}\left(\tau_{\rho}, \tau_{e}, \tau_{\varepsilon}, \tau_{j}, \tau_{q}, \tau_{j}, \tau_{q}, \tau_{s}, \tau_{s}\right)^{-1}, \tag{2.21}$$

where τ_i denotes the relaxation time for the *i*th moment in \boldsymbol{m} . τ_ρ and τ_j are related to mass and momentum, respectively, and are given by $\tau_\rho = \tau_j = 1$. τ_e and τ_ε are related to internal energy, and have insignificant impacts for an isothermal system; their values are referred to Guo et al. [49]: $\tau_e = 1.1$, and $\tau_\varepsilon = 1.2$. τ_s is related to shear viscosity, μ . To reflect the impact of Knudsen layer [50, 51], which is formed due to frequent collisions between fluid molecules and walls in confined space, on fluid viscosity, the effective viscosity model [52, 53] is used, in which τ_s is expressed as

$$\tau_s = \frac{1}{2} + \sqrt{\frac{6}{\pi}} \frac{NKn}{1 + 2Kn},\tag{2.22}$$

where $N=H/\delta x$ is the lattice number along the characteristic length. τ_q is

related to slip velocity and will be discussed in the following subsection.

 f_i^{eq} is the equilibrium distribution function given by [54]

$$f_i^{\text{eq}} = w_i \rho \left[1 + \frac{e_i \cdot u}{(c_s)^2} + \frac{(e_i \cdot u)^2}{2(c_s)^4} - \frac{u \cdot u}{2(c_s)^2} \right],$$
 (2.23)

where w_i is the weighting factor with $w_0 = 4/9$, $w_{1\sim 4} = 1/9$, and $w_{5\sim 8} = 1/36$, $c_s = c/\sqrt{3}$ is the sound of speed, and ρ and \boldsymbol{u} are macroscopic density and velocity, respectively. ρ and \boldsymbol{u} are related to the distribution function, given as $\rho = \sum_i f_i$, and $\rho \boldsymbol{u} = \sum_i e_i f_i + \frac{\delta t}{2} \boldsymbol{G}$.

The forcing term is also expressed in the moment space accordingly [49, 53]:

$$\boldsymbol{F} = \boldsymbol{M}^{-1} \left(\boldsymbol{I} - \frac{1}{2} \boldsymbol{S} \right) \boldsymbol{M} \bar{\boldsymbol{F}}, \tag{2.24}$$

where $\boldsymbol{F} = \boldsymbol{F}\left(\boldsymbol{x},t\right) = \left(F_0, F_1, ..., F_8\right)^T$, and $\bar{\boldsymbol{F}} = \left(\bar{F}_0, \bar{F}_1, ..., \bar{F}_8\right)$ with

$$\bar{F}_i = w_i \left[\frac{\boldsymbol{e}_i \cdot \boldsymbol{G}}{c_s^2} + \frac{\boldsymbol{u}\boldsymbol{G} : \left(\boldsymbol{e}_i \boldsymbol{e}_i - c_s^2 \boldsymbol{I} \right)}{c_s^4} \right]. \tag{2.25}$$

2.2.2. Boundary Conditions

The combined half-way bounce-back and specular reflection boundary condition is used to represent the boundary condition:

$$f_i = rf_i^{\text{BB}} + (1 - r)f_i^{\text{SR}},$$
 (2.26)

where r is the contribution of the half-way bounce-back part to the combination, f_i^{BB} , f_i^{SR} are the distribution functions calculated using half-way bounce-back and specular reflection schemes, respectively.

Parameters r and τ_q are chosen such that the slip velocity obtained from LBM matches the macroscopic second-order slip boundary condition [55]:

$$u_s = C_1 K n \frac{\partial u}{\partial n} \bigg|_w - C_2 K n^2 \frac{\partial^2 u}{\partial n^2} \bigg|_w, \qquad (2.27)$$

where C_1 and C_2 are slip coefficients, n is the wall normal coordinate, and the subscript w denotes the quantity at the wall. r and τ_q are expressed as [49]

$$r = \frac{1}{1 + C_1 \sqrt{\frac{6}{\pi}}},\tag{2.28}$$

and

$$\tau_q = \frac{1}{2} + \frac{3 + \pi (2\tau_s - 1)^2 C_2}{8(2\tau_s - 1)},$$
(2.29)

where C_1 and C_2 are given by $C_1 = 1.0 - 0.1817\sigma$ ($\sigma = 1$ for fully diffusive), and $C_2 = 0.8$ [53].

2.2.3. Fluid-fluid and Fluid-solid Interactions

To account for the intermolecular forces which contribute to the non-ideal behavior of confined fluid, a long-range interaction force between particles is introduced [21]:

$$\mathbf{F}_{\mathrm{ff}}(\mathbf{x},t) = -c_0 G_{\mathrm{ff}} \psi(\mathbf{x},t) \sum_i w_i' \psi(\mathbf{x} + \mathbf{e}_i \delta t, t) \mathbf{e}_i, \qquad (2.30)$$

where $G_{\rm ff}$ is the intermolecular strength, $\psi\left(\boldsymbol{x},t\right)$ is the pseudopotential function defined as a function of fluid density, ρ , w_i' is the weighting factor with $w_0'=0$, $w_{1\sim4}'=1/3$, and $w_{5\sim8}'=1/12$, and c_0 is a constant depending on the lattice structure. In the case of D2Q9 model, $c_0=6.0$. Incorporation of interaction forces between particles lead to a non-ideal EOS given by [25]

$$P = \frac{\rho}{3} + \frac{c_0}{2} G_{\rm ff} \psi^2. \tag{2.31}$$

Different forms of ψ may lead to different EOS. In this work, the mEPR-EOS is incorporated into the LBM. Following Yuan and Schaefer [25], P is expressed

as a function of ρ and T by substituting $v = 1/\rho$ into Eq. (2.12):

$$P = \frac{\rho RT}{1 - b'\rho} - \frac{(a' - c')\rho^2}{1 + 2b'\rho - b'^2\rho^2}.$$
 (2.32)

Combining Eqs. (2.31) and (2.32), the corresponding pseudopotential function is derived:

$$\psi = \sqrt{\frac{2}{c_0 G_{\rm ff}} \left(\frac{\rho RT}{1 - b'\rho} - \frac{(a' - c')\rho^2}{1 + 2b'\rho - b'^2\rho^2} - \frac{\rho}{3} \right)}.$$
 (2.33)

The interaction between particles and walls is given in a similar form [22]:

$$F_{\text{fw}}(\boldsymbol{x},t) = -G_{\text{fw}}\psi(\boldsymbol{x},t)\sum_{i}w_{i}'s\left(\boldsymbol{x} + \boldsymbol{e}_{i}\delta t, t\right)\boldsymbol{e}_{i}, \qquad (2.34)$$

where G_{fw} is the adsorptive strength, and s is the switch function, which is equal to 1 if $(x + e_i \delta t)$ is solid wall, and equal to 0 if otherwise. It ensures that the adsorptive force only applies to particles near solid walls.

2.3. Unit Conversion

Lattice units are used in LBM simulations. As mentioned by Xu et al. [29], the choice of values of parameters, e.g., a and b, is relatively arbitrary except for stability considerations. This work follows the recommendation of Yuan and Schaefer [25]:

$$a^{lu} = \frac{2}{49}, \ b^{lu} = \frac{2}{21}, \text{ and } R^{lu} = 1.$$
 (2.35)

Critical pressure, temperature, and density at bulk condition in lattice units, P_{cb}^{lu} , T_{cb}^{lu} , and ρ_{cb}^{lu} (superscript 'lu' denotes property in lattice units), are obtained by combining Eqs. (2.1)-(2.3) and (2.35).

To relate these properties to physical units, the reduced properties are used:

$$P_r = \frac{P}{P_c}, T_r = \frac{T}{T_c}, \text{ and } \rho_r = \frac{\rho}{\rho_c},$$
 (2.36)

where subscripts r and c denote reduced and critical property, respectively.

According to the law of corresponding states [56], the reduced properties should be the same in lattice and physical units. Therefore, P_r is expressed as

$$P_r = \frac{P^{\text{lu}}}{P_c^{\text{lu}}} = \frac{P^{\text{pu}}}{P_c^{\text{pu}}},$$
 (2.37)

where superscript 'pu' denotes property in physical units. Eq. (2.37) gives

$$P^{\mathrm{pu}} = \frac{P^{\mathrm{lu}}}{P_{c}^{\mathrm{lu}}} \cdot P_{c}^{\mathrm{pu}}. \tag{2.38}$$

Based on Eq. (2.38), the pressure in lattice units are converted to the pressure in physical units. Similarly, relations between lattice and physical units for T and ρ could be derived.

3. Proposed Model

3.1. Motivation

Reference data used in this study are from work by Sobecki et al. [41]. The reference data consist of density phase diagram for methane under various confinement of H = 5nm, 3nm, and 2nm. This data is based on MD simulation using the GEMC NVT method, where N, V, and T denote the total number of molecules, the total volume, and temperature, respectively. Readers are referred to Sobecki et al. [41] for details. The corresponding shift of critical pressure and temperature, and the deviation of shift, computed as the ratio of absolute value of difference between the shift of critical pressure and temperature over the shift of critical temperature, are presented in Fig. 1. As shown, the magnitude of

the shift for critical pressure and temperature decreases with additional confinement, indicating that critical pressure and temperature decreases as the pore width becomes narrower. For a given pore width, the shift in critical pressure is larger than the shift in critical pressure, implying that Eq. (2.11) may not be appropriate in describing the shift in critical properties for such systems.

In this work, the saturated pressure of the vapor phase, obtained from the GEMC NVT simulation data, is used as the primary variable to solve for saturated densities of vapor and liquid phases using different forms of EOS. The density phase diagram at different pore widths are presented in Fig. 2. Polylines with circles denote bulk values extracted from the National Institute Standards and Technology database website [57]. The evenly spaced polylines with circles denote results obtained from the GEMC NVT simulation. It is observed that the phase envelop is suppressed in the confined space. Compared to the bulk values at the same temperature, the saturated vapor density increases meanwhile the saturated liquid density is reduced. Solutions from the EPR-EOS, as denoted by the evenly spaced polylines with triangles, appear to capture the shift of critical temperature as they approach the reference data near the critical point.

To quantify the differences between solutions of EOS and the reference data, deviations are computed and results are presented in Fig. 3. Results obtained from solutions of EPR-EOS show that deviations of liquid phase are more pronounced than those of vapor phase across the investigated pore widths. It is worth noting that below the critical point, the two phases, i.e., vapor and liq-

uid, are considered to exist at different pressures separated by the capillary pressure in confined spaces. The saturated vapor pressure is used to solve for saturated densities of vapor and liquid phases simultaneously. This may lead to relatively large deviations for the liquid phase. In addition, for a given pore width, deviations of the liquid phase decrease as temperature increases. This effect is especially noticeable near the critical point for pore width of 5nm and 3nm. This observation may be attributed to the fact that the pressure difference between vapor and liquid phases becomes less pronounced as temperature increases. At critical point, capillary pressure vanishes and the saturated pressure of the vapor phase match that of the liquid phase.

3.2. Formulation

We propose a region-dependent view, in which parameter β has the following expression:

$$\beta = \begin{cases} \frac{P_{cr}}{T_{cr}} \cdot \gamma, & \text{in the two-phase region,} \\ \frac{P_{cr}}{T_{cr}}, & \text{otherwise,} \end{cases}$$
 (3.1)

where γ is introduced to account for the existence of capillary pressure in the two-phase region. On the other hand, capillary pressure does not exist outside the two-phase region. Under such a condition, β is used to correct the critical pressure only; it is computed as the ratio of the shift of the critical pressure over that of the critical temperature based on the reference data. As aforementioned, inside the two-phase region, the deviation of liquid phase density appears to depend on the reduced temperature. Motivated by this observation, we propose

the following expression for γ :

$$\gamma = m^{(T_r - T_{cr})},\tag{3.2}$$

where m is a coefficient determined by benchmarking solutions of mEPR-EOS against the reference data. It is noted that as $T \to T_c$, $T_r \to T_{cr}$, and in the limiting case:

$$\lim_{T_r \to T_{cr}} \gamma = 1. \tag{3.3}$$

Eq. (3.3) implies that near the critical point, value of γ approaches unity, and therefore, β is continuous across the entire region.

Through investigations with different values of m, we find that solutions of mEPR-EOS obtained with m=1.38 best fit the reference data. As shown in Fig. 2, solutions from the mEPR-EOS follow the reference data for both vapor and liquid phases closely across the investigated cases. In fact, compared to EPR-EOS, the use of mEPR-EOS reudces the overall error from 19.42% to 5.87%.

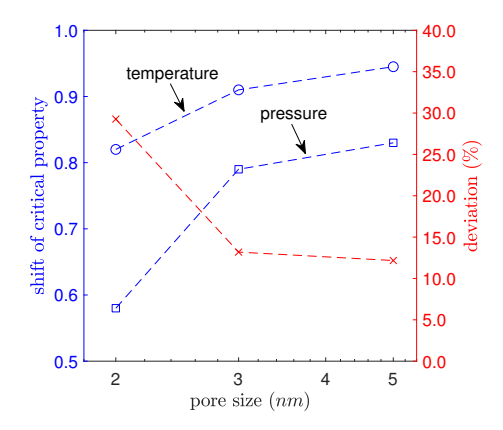


Figure 1: Shift of critical properties versus pore width.

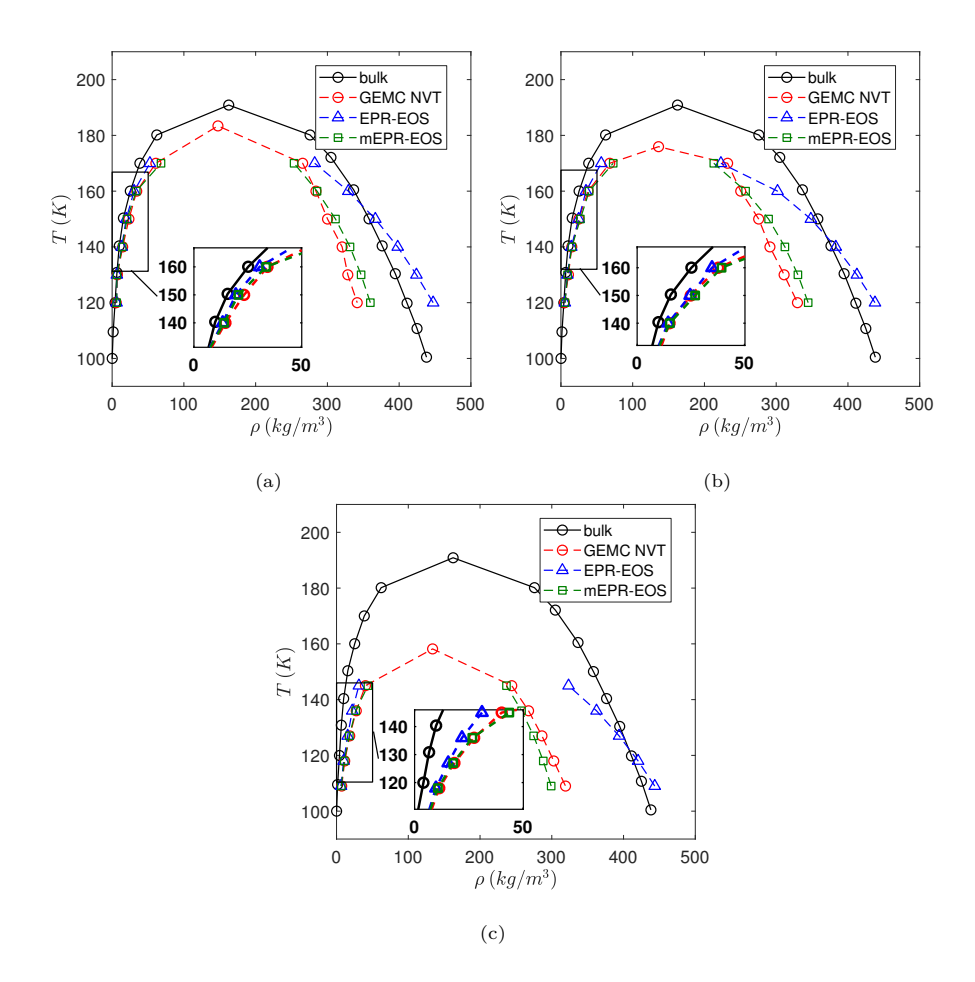


Figure 2: Comparison of density phase diagram using different methods. Pore width is given by (a) 5nm, (b) 3nm, and (c) 2nm.

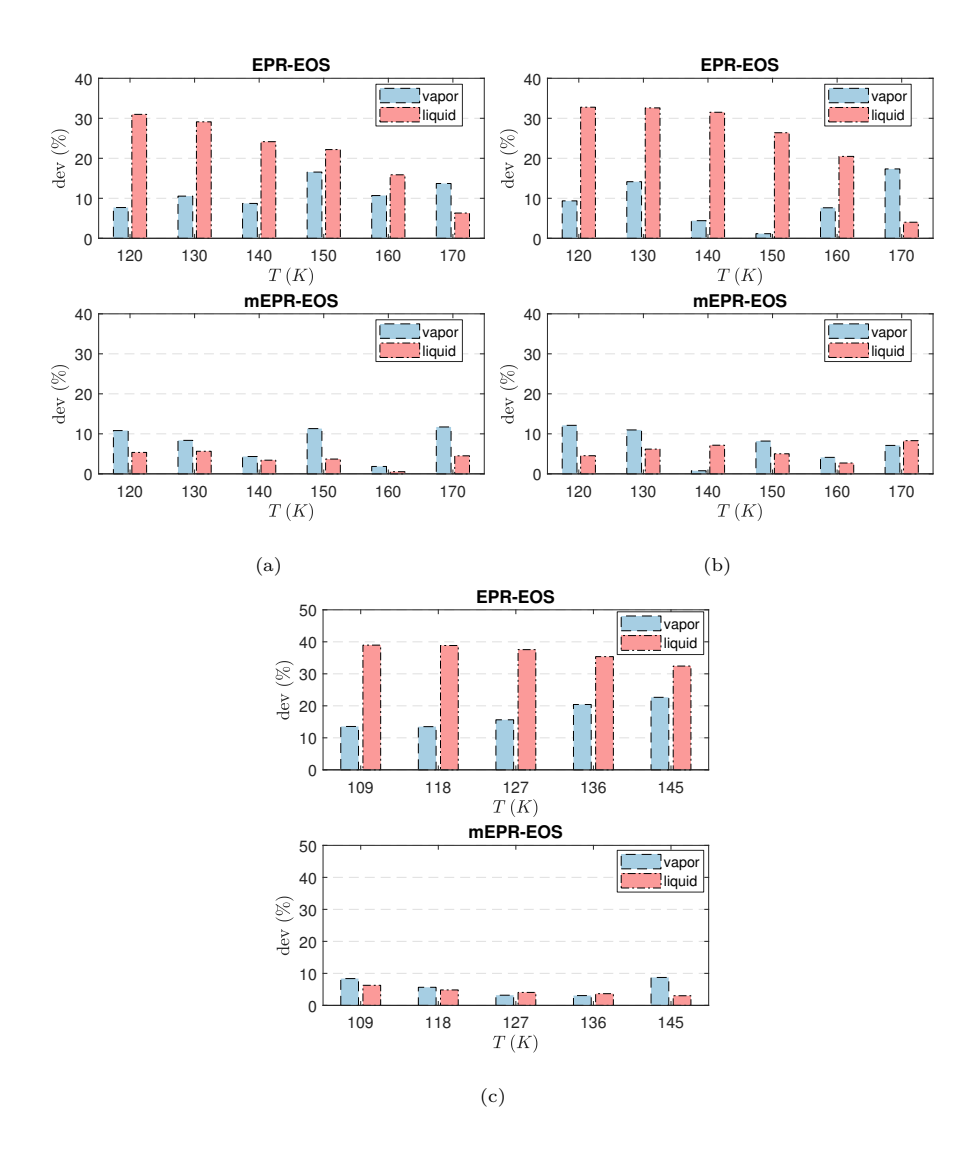


Figure 3: Comparison of deviation of density data using EPR-EOS and mEPR-EOS. Pore width is given by (a) 5nm, (b) 3nm, and (c) 2nm.

4. Results and Discussions

4.1. Sensitivity Analysis

In general, methane is stored in unconventional reservoirs at temperatures higher than its critical point. Therefore, single phase (gas) or supercritical fluid flow dominate transport in such systems. As such, we start this section by presenting the impact of confinement on the density of methane at temperatures higher than T_{cb} . Two values of temperature, i.e., T=229K and 298K, are investigated. In each case, values of density are obtained by solving the mEPR-EOS with confined systems of different pore widths.

Fig. 4 shows the density of methane versus pressure at bulk condition and under confinement. It is observed that at small pressures, differences between the bulk density data and solutions from mEPR-EOS are insignificant. At larger pressures, however, density curves start to diverge. At a relatively large pressure, densities under confinement are smaller than that of the bulk data, and an additional confinement leads to a larger reduction of densities. Moreover, given the same pressure, a decrease of density caused by confinement is more prominent at a lower temperature (i.e., 229K in Fig. 4a) due to weaker intermolecular interactions. These observations indicate that density is more likely to be influenced by confinement effects in a system with lower temperatures and higher pressures.

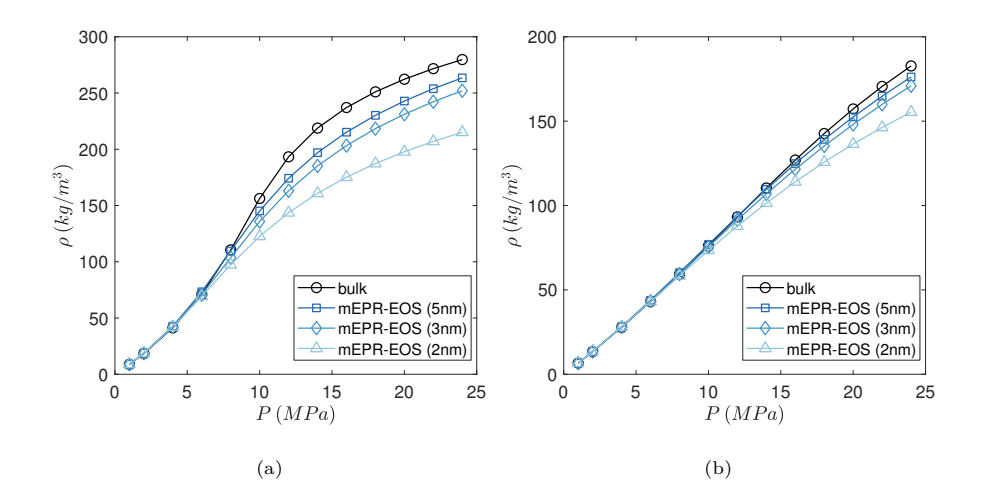


Figure 4: Density of methane at different confined systems. System temperature is given by (a) 229K, and (b) 298K.

4.2. Methane Flow in Slit Nanopores

In this section, we couple mEPR-EOS with MRT-LBM to study the effects of confinement on transport. Flow is simulated in a two-dimensional slit pore driven by a constant external force, and periodic boundary condition is applied in the streamwise direction. Simulation domain is discretized by a uniform lattice with a resolution of 0.1nm/lu. The mesh size is given by $101 \times N_y$, where N_y is the number of grid depending on the pore width, which is given by 51, 31, and 21 for H = 5nm, 3nm, and 2nm, respectively. The system temperature is fixed at 298K, and two values of pressure are investigated: 0.5MPa and 2.0Mpa.

4.2.1. Adsorption Behavior

Unlike the bulk fluid, the spatial density distribution of methane inside the slit pore is not homogeneous due to interactions between fluids and walls. Density near the wall is higher than that in the middle of the pore. The adsorptive strength (G_{fw}) is determined by matching the density ratio, defined as the ratio of density located near the wall and at the centerline of the pore, obtained using LBM with that from MD simulation at the same pressure and temperature. Here density profiles from the work by Yu et al. [17] are used as references - see Fig. 5. As shown, half (the left part) of the density profile is presented due to symmetry. The position is nondimensionalized such that the location of the highest density value is equal to -1.0. It is observed that predictions from LBM follow those obtained from MD simulation.

To gain more insight into coupling of EOS and adsorption behavior, PR-EOS is also incorporated into the LBM and the corresponding $G_{\rm fw}$ is determined based on the density ratio from reference data. Fig. 6 shows comparisons of absolute values of the adsorptive strength; given the same pore width and EOS, $|G_{\rm fw}|$ is larger at P=2MPa than P=0.5MPa due to a higher density ratio. Moreover, in systems with identical pressures, $|G_{\rm fw}|$ is larger in the case where mEPR-EOS is used. This is because incorporating mEPR-EOS leads to stronger adsorptive forces between particles than PR-EOS. Therefore, to obtain the same density ratio, $|G_{\rm fw}|$ needs to be increased to enhance the interactions between particles and walls.

4.2.2. Transport Characteristics

The steady-state velocity profiles obtained from LBM simulations, in which PR-EOS and mEPR-EOS are coupled independently, are presented in Fig. 7. Incorporating mEPR-EOS leads to a significant reduction of velocity compared

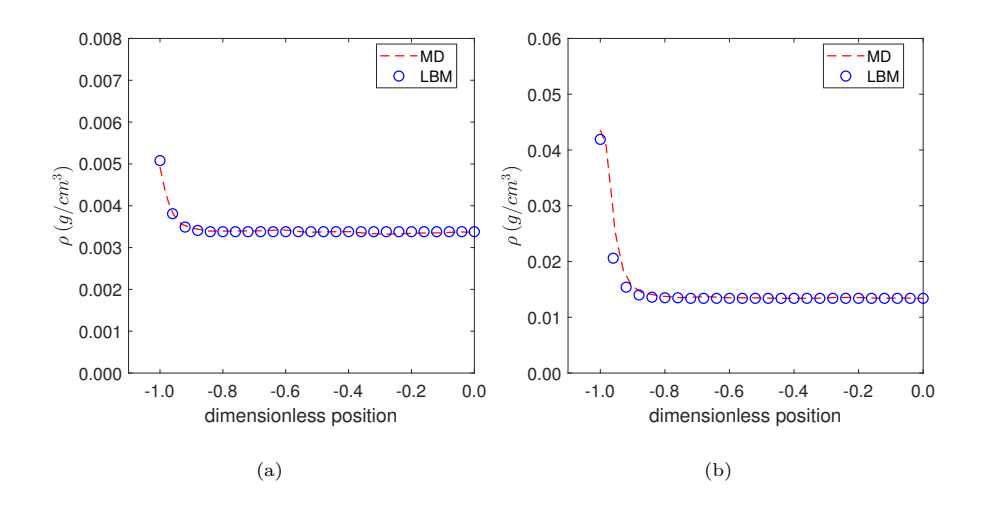


Figure 5: Density profiles of methane in slit pores. System pressure is given by (a) 0.5MPa, and (b) 2.0MPa.

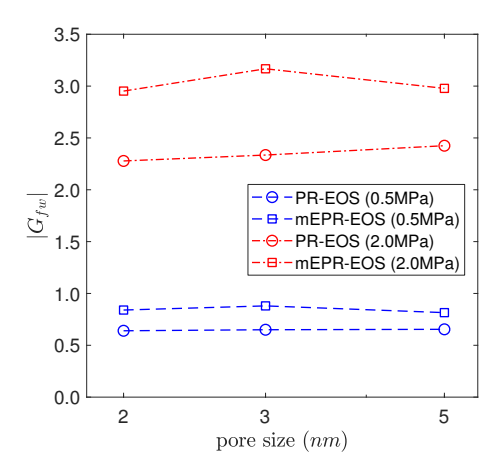


Figure 6: Comparison of absolute value of adsorptive strength in different systems.

to that of PR-EOS due to stronger interparticle forces. In addition, velocity profile obtained from the use of mEPR-EOS exhibits a smaller curvature, indicating that coupling mEPR-EOS may lead to a larger fluid viscosity compared to PR-EOS.

The velocity profile partially reveals the flow characteristics: the parabolic velocity profile is attributed to the viscous flow, and the nonzero velocity near the wall is caused by the Knudsen diffusion. In spite of that, the transport mechanism is not fully revealed due to nonuniform distribution of density in the direction perpendicular to the mean flow. Therefore, mass flux, defined as the product of velocity and density, is used to further investigate transport. Fig. 8a shows mass flux profiles in different systems using mEPR-EOS. In Fig. 8a, the profile shape is no longer parabolic; mass flux near the wall is higher than that in the bulk region, which is referred to as surface diffusion. To better understand the interplay of different transport mechanisms on mass flux, contribution from each component is quantified given a mass flux profile. An example is shown in Fig. 8b, where the mass flux profile is extracted from the result of H = 2nm and P = 2MPa.

Fig. 9 shows the mass flux contributions from three transport mechanisms. Under relatively low pressure (P=0.5MPa), Knudsen diffusion is the primary transport mechanism due to frequent collisions between molecules and walls. Contribution from Knudsen diffusion is insensitive to pore size. It is also observed that contribution from surface diffusion decreases as the pore widens. As a result, the ratio of viscous flow increases and exceeds that of the surface

diffusion. On the other hand, in systems with P=2.0MPa, an increase of pore size leads to a larger contribution from viscous flow while contributions of surface and Knudsen diffusion diminish.

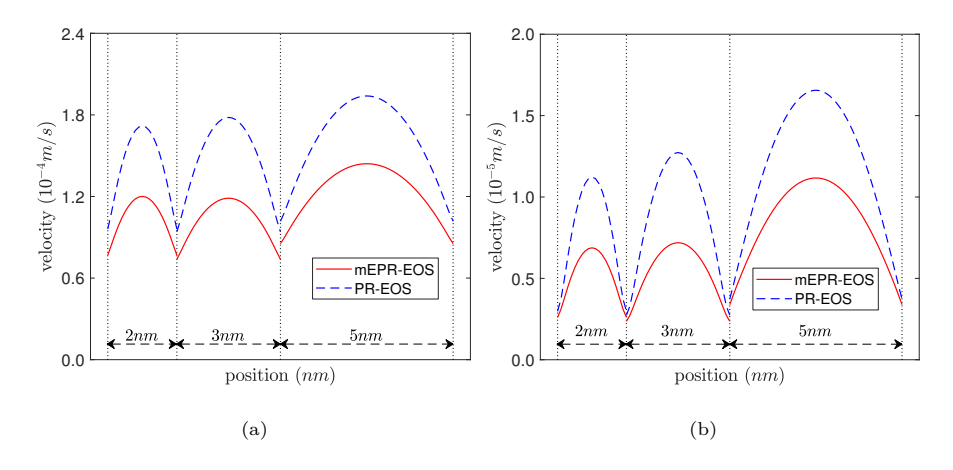


Figure 7: Velocity profiles of methane in slit nanopores with different pore widths. System pressure is given by (a) 0.5MPa, and (b) 2.0MPa.

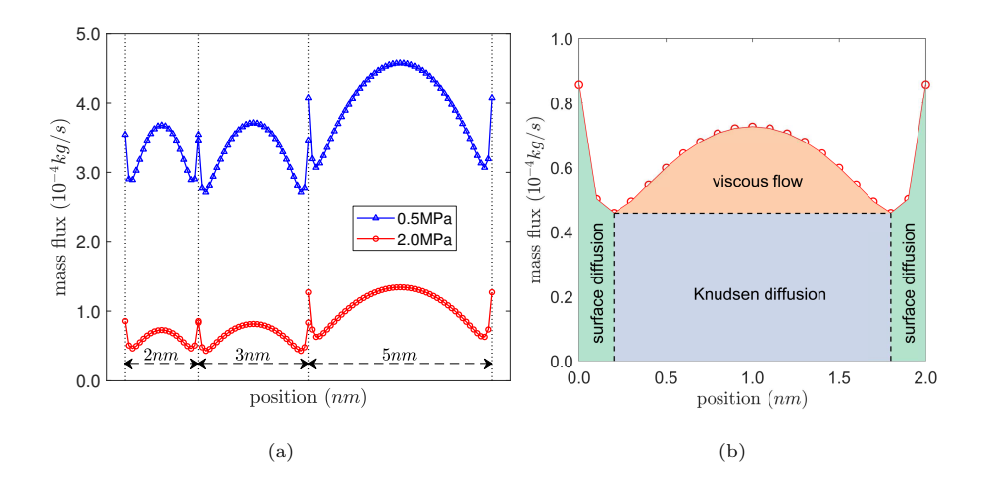


Figure 8: Mass flux profiles of methane in slit nanopores. (a) Comparison of mass flux profiles at different pressure and pore width, and (b) schematic of mass flux ratio from different transport mechanisms.

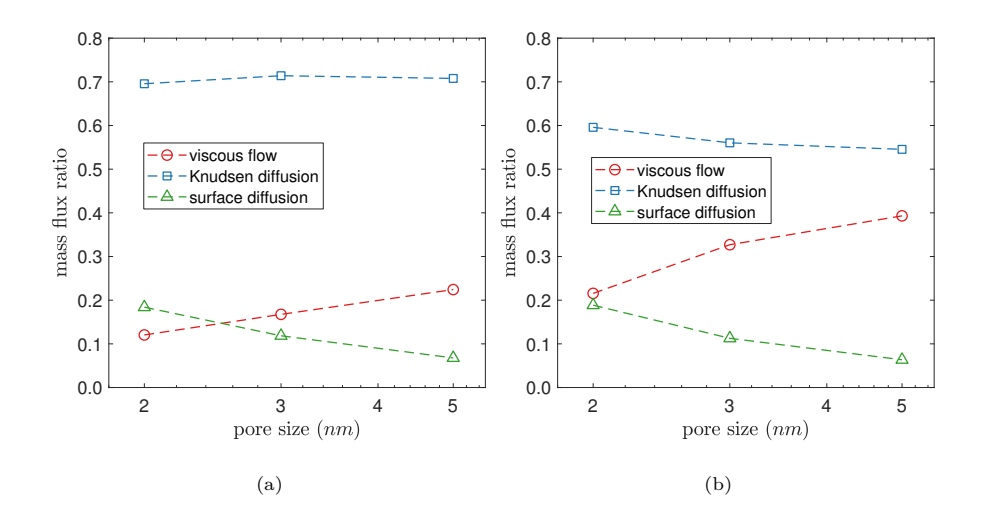


Figure 9: Mass flux contributions from different transport mechanisms. System pressure is given by (a) 0.5MPa, and (b) 2.0MPa.

5. Conclusion

In this work, a modified extension of PR-EOS is developed to describe phase behavior of methane in confined nanopores. This modified formulation, referred to as mEPR-EOS, is motivated and guided by data from a series of MD simulation runs using the GEMC NVT method [41]. This data (reference data) include the shift of critical properties and the saturated phase density. Similar to a prior extension to PR-EOS (EPR-EOS) [45], the shift of critical temperature under confinement is taken into account by modifying the parameter associated with attractive forces in the PR-EOS. In terms of the shift of critical pressure, a phase region-dependent parameter is proposed. This parameter is treated as a constant outside the two-phase region; its value is determined based on the shift of critical pressure from the reference data. In two-phase region, this parameter

eter is expressed as a product of that constant and a temperature dependent coefficient, which is introduced to account for the existence of capillary pressure between vapor and liquid phases. To verify the proposed formulation, we compare numerical solutions of EPR-EOS and mEPR-EOS with the reference data that describe the saturated phase density at different pore sizes. Results show that mEPR-EOS outperforms EPR-EOS and it follows the reference data closely.

The proposed mEPR-EOS is incorporated in MRT-LBM to study the impact of confined phase behavior on transport in slit nanopores. A combined half-way bounce back and specular reflection is used to capture the slip velocity. Interactions between fluid particles, as well as fluid particles and walls, are incorporated in the form of external forces. The adsorptive strength between fluid particles and walls is determined based on the density profile from MD simulation results. Results indicate that values of the adsorptive strength is affected by the form of EOS: the use of mEPR-EOS leads to a larger absolute value than that of using PR-EOS. This is due to stronger interactions between fluid particles under confinement. In addition, compared to PR-EOS, mEPR-EOS results in smaller fluid velocities. The transport characteristics are investigated based on the mass flue profile by quantifying contributions from different transport mechanisms, namely viscous flow, Knudsen diffusion, and surface diffusion. In the system under a relatively low pressure (P = 0.5MPa), transport appears to be dominated by Knudsen diffusion: the contribution from Knudsen diffusion is approximately 70% across different pore widths. Under a higher pressure (P=2.0MPa), the relative influence of various flow mechanisms is affected by the pore size. The contribution from viscous flow increases as the pore widens while the influence of the other two mechanisms diminishes. This observation indicates that pressure plays an important role in determining the impact of pore size on transport characteristics in confined systems.

Acknowledgments

This work was supported as part of the Center for Mechanistic Control of Water-Hydrocarbon-Rock Interactions in Unconventional and Tight Oil Formations (CMC-UF), an Energy Frontier Research Center funded by the U.S. Department of Energy, Office of Science under DOE (BES) Award DE-SC0019165. The authors are grateful to Dr. Carlos Nieto-Draghi and his colleagues at Institut Français du Pétrole Energies nouvelles for sharing data and for our lively discussion.

References

- M. Karimi-Fard, L. J. Durlofsky, K. Aziz, An efficient discrete fracture model applicable for general purpose reservoir simulators, SPE J. 9 (2004) 227–236.
- [2] L. Li, S. H. Lee, Efficient field-scale simulation of black oil in a naturally fractured reservoir through discrete fracture networks and homogenized media, SPE Reservoir Eval. Eng. 11 (2008) 750–758.

- [3] A. Moinfar, A. Varavei, K. Sepehrnoori, R. T. Johns, Development of an efficient embedded discrete fracture model for 3D compositional reservoir simulation in fractured reservoirs, SPE J. 19 (2014) 289–303.
- [4] J. Jiang, R. M. Younis, A multimechanistic multicontinuum model for simulating shale gas reservoir with complex fractured system, Fuel 161 (2015) 333–344.
- [5] Y. Wang, M. Shahvali, Discrete fracture modeling using Centroidal Voronoi grid for simulation of shale gas plays with coupled nonlinear physics, Fuel 163 (2016) 65–73.
- [6] M. Ţene, S. B. Bosma, M. S. Al Kobaisi, H. Hajibeygi, Projection-based embedded discrete fracture model (pEDFM), Adv. Water Resour. 105 (2017) 205–216.
- [7] M. A. Biot, General theory of three-dimensional consolidation, J. Appl. Phys. 12 (1941) 155–164.
- [8] J. Kim, G. J. Moridis, Gas flow tightly coupled to elastoplastic geomechanics for tight-and shale-gas reservoirs: Material failure and enhanced permeability, SPE J. 19 (2014) 1–110.
- [9] P. Cao, J. Liu, Y.-K. Leong, A fully coupled multiscale shale deformationgas transport model for the evaluation of shale gas extraction, Fuel 178 (2016) 103–117.
- [10] I. Y. Akkutlu, Y. Efendiev, M. Vasilyeva, Y. Wang, Multiscale model

- reduction for shale gas transport in poroelastic fractured media, J. Comput. Phys. 353 (2018) 356–376.
- [11] R. G. Loucks, R. M. Reed, S. C. Ruppel, D. M. Jarvie, Morphology, genesis, and distribution of nanometer-scale pores in siliceous mudstones of the Mississippian Barnett Shale, J. Sediment. Res. 79 (2009) 848–861.
- [12] S. M. Kang, E. Fathi, R. J. Ambrose, I. Y. Akkutlu, R. F. Sigal, Carbon dioxide storage capacity of organic-rich shales, Spe J. 16 (2011) 842–855.
- [13] S. Saraji, M. Piri, The representative sample size in shale oil rocks and nano-scale characterization of transport properties, Int. J. Coal Geol. 146 (2015) 42–54.
- [14] A. Zolfaghari, H. Dehghanpour, M. Xu, Water sorption behaviour of gas shales: II. Pore size distribution, Int. J. Coal Geol. 179 (2017) 187–195.
- [15] K. Falk, B. Coasne, R. Pellenq, F.-J. Ulm, L. Bocquet, Subcontinuum mass transport of condensed hydrocarbons in nanoporous media, Nat. Commun. 6 (2015) 6949.
- [16] S. Riewchotisakul, I. Y. Akkutlu, Adsorption-enhanced transport of hydrocarbons in organic nanopores, SPE J. 21 (2016) 1960–1969.
- [17] H. Yu, J. Fan, J. Chen, Y. Zhu, H. Wu, Pressure-dependent transport characteristic of methane gas in slit nanopores, Int. J. Heat Mass Transfer 123 (2018) 657–667.

- [18] Y. Wang, S. A. Aryana, Pore-scale simulation of gas flow in microscopic permeable media with complex geometries, J. Nat. Gas Sci. Eng. (2020) 103441.
- [19] G. R. McNamara, G. Zanetti, Use of the Boltzmann equation to simulate lattice-gas automata, Phys. Rev. Lett. 61 (1988) 2332.
- [20] S. Chen, G. D. Doolen, Lattice Boltzmann method for fluid flows, Annu. Rev. Fluid Mech. 30 (1998) 329–364.
- [21] X. Shan, H. Chen, Lattice Boltzmann model for simulating flows with multiple phases and components, Phys. Rev. E 47 (1993) 1815.
- [22] M. C. Sukop, D. Or, Lattice Boltzmann method for modeling liquid-vapor interface configurations in porous media, Water Resour. Res. 40 (2004).
- [23] E. Fathi, I. Y. Akkutlu, Lattice Boltzmann method for simulation of shale gas transport in kerogen, Spe J. 18 (2012) 27–37.
- [24] Y. Ning, Y. Jiang, H. Liu, G. Qin, Numerical modeling of slippage and adsorption effects on gas transport in shale formations using the lattice Boltzmann method, J. Nat. Gas Sci. Eng. 26 (2015) 345–355.
- [25] P. Yuan, L. Schaefer, Equations of state in a lattice Boltzmann model, Phys. Fluids 18 (2006) 042101.
- [26] H. Yu, J. Chen, Y. Zhu, F. Wang, H. Wu, Multiscale transport mechanism of shale gas in micro/nano-pores, Int. J. Heat Mass Transfer 111 (2017) 1172–1180.

- [27] D. Y. Peng, D. B. Robinson, A new two-constant equation of state, Ind. Eng. Chem. Fundam. 15 (1976) 59–64.
- [28] J. Zhao, J. Yao, L. Zhang, H. Sui, M. Zhang, Pore-scale simulation of shale gas production considering the adsorption effect, Int. J. Heat Mass Transfer 103 (2016) 1098–1107.
- [29] R. Xu, M. Prodanović, C. J. Landry, Study of subcritical and supercritical gas adsorption behavior in different nanopore systems in shale using lattice Boltzmann method, Int. J. Coal Geol. 212 (2019) 103263.
- [30] X. Liu, D. Zhang, A review of phase behavior simulation of hydrocarbons in confined space: Implications for shale oil and shale gas, J. Nat. Gas Sci. Eng. (2019) 102901.
- [31] B. Nojabaei, R. T. Johns, L. Chu, Effect of capillary pressure on phase behavior in tight rocks and shales, SPE Reservoir Eval. Eng. 16 (2013) 281–289.
- [32] D. R. Sandoval, W. Yan, M. L. Michelsen, E. H. Stenby, The phase envelope of multicomponent mixtures in the presence of a capillary pressure difference, Ind. Eng. Chem. Res. 55 (2016) 6530–6538.
- [33] T. W. Teklu, N. Alharthy, H. Kazemi, X. Yin, R. M. Graves, A. M. Al-Sumaiti, Phase behavior and minimum miscibility pressure in nanopores, SPE Reservoir Eval. Eng. 17 (2014) 396–403.
- [34] X. Dong, H. Liu, J. Hou, K. Wu, Z. Chen, Phase equilibria of confined

- fluids in nanopores of tight and shale rocks considering the effect of capillary pressure and adsorption film, Ind. Eng. Chem. Res. 55 (2016) 798–811.
- [35] J. Y. Zuo, X. Guo, Y. Liu, S. Pan, J. Canas, O. C. Mullins, Impact of capillary pressure and nanopore confinement on phase behaviors of shale gas and oil, Energy Fuels 32 (2018) 4705–4714.
- [36] G. J. Zarragoicoechea, V. A. Kuz, Critical shift of a confined fluid in a nanopore, Fluid Phase Equilib. 220 (2004) 7–9.
- [37] A. Vishnyakov, E. Piotrovskaya, E. Brodskaya, E. Votyakov, Y. K. Tovbin, Critical properties of Lennard-Jones fluids in narrow slit-shaped pores, Langmuir 17 (2001) 4451–4458.
- [38] S. K. Singh, J. K. Singh, Effect of pore morphology on vapor-liquid phase transition and crossover behavior of critical properties from 3D to 2D, Fluid Phase Equilib. 300 (2011) 182–187.
- [39] T. Pitakbunkate, P. B. Balbuena, G. J. Moridis, T. A. Blasingame, Effect of confinement on pressure/volume/temperature properties of hydrocarbons in shale reservoirs, SPE J. 21 (2016) 621–634.
- [40] B. Jin, R. Bi, H. Nasrabadi, Molecular simulation of the pore size distribution effect on phase behavior of methane confined in nanopores, Fluid Phase Equilib. 452 (2017) 94–102.
- [41] N. Sobecki, C. Nieto-Draghi, A. Di Lella, D. Y. Ding, Phase behavior of hydrocarbons in nano-pores, Fluid Phase Equilib. 497 (2019) 104–121.

- [42] A. Z. Panagiotopoulos, Direct determination of phase coexistence properties of fluids by Monte Carlo simulation in a new ensemble, Mol. Phys. 61 (1987) 813–826.
- [43] A. Z. Panagiotopoulos, N. Quirke, M. Stapleton, D. Tildesley, Phase equilibria by simulation in the Gibbs ensemble: alternative derivation, generalization and application to mixture and membrane equilibria, Mol. Phys. 63 (1988) 527–545.
- [44] E. G. Derouane, On the physical state of molecules in microporous solids, Microporous Mesoporous Mater. 104 (2007) 46–51.
- [45] G. Yang, Z. Fan, X. Li, Determination of confined fluid phase behavior using extended Peng-Robinson equation of state, Chem. Eng. J. 378 (2019) 122032.
- [46] X. He, L.-S. Luo, Theory of the lattice Boltzmann method: From the Boltzmann equation to the lattice Boltzmann equation, Phys. Rev. E 56 (1997) 6811.
- [47] P. Lallemand, L.-S. Luo, Theory of the lattice Boltzmann method: dispersion, dissipation, isotropy, Galilean invariance, and stability, Phys. Rev. E 61 (2000) 6546.
- [48] D. d'Humières, Multiple-relaxation-time lattice Boltzmann models in three dimensions, Philosophical Transactions of the Royal Society of London. Series A: Mathematical, Physical and Engineering Sciences 360 (2002) 437– 451.

- [49] Z. Guo, C. Zheng, B. Shi, Lattice Boltzmann equation with multiple effective relaxation times for gaseous microscale flow, Phys. Rev. E 77 (2008) 036707.
- [50] D. A. Lockerby, J. M. Reese, M. A. Gallis, Capturing the knudsen layer in continuum-fluid models of nonequilibrium gas flows, AIAA J. 43 (2005) 1391–1393.
- [51] D. A. Lockerby, J. M. Reese, M. A. Gallis, The usefulness of higher-order constitutive relations for describing the Knudsen layer, Phys. Fluids 17 (2005) 100609.
- [52] V. K. Michalis, A. N. Kalarakis, E. D. Skouras, V. N. Burganos, Rarefaction effects on gas viscosity in the knudsen transition regime, Microfluid. Nanofluid. 9 (2010) 847–853.
- [53] Q. Li, Y. He, G. Tang, W. Tao, Lattice Boltzmann modeling of microchannel flows in the transition flow regime, Microfluid. Nanofluid. 10 (2011) 607–618.
- [54] H. Chen, S. Chen, W. H. Matthaeus, Recovery of the Navier-Stokes equations using a lattice-gas Boltzmann method, Phys. Rev. A 45 (1992) R5339.
- [55] G. E. Karniadakis, A. Beskok, Micro flows: fundamentals and simulation, Springer, 2002.
- [56] E. A. Guggenheim, The principle of corresponding states, J. Chem. Phys. 13 (1945) 253–261.

[57] P. J. Linstrom, W. G. Mallard (Eds.), NIST Chemistry WebBook, NIST Standard Reference Database Number 69, National Institute of Standards and Technology, Gaithersburg MD, 20899, 2020.